Key Parameters for Detectivity Improvement of Low Noise Anisotropic Magnetoresistive Sensors Made of La 2/3 Sr 1/3 MnO 3 Single Layers on Vicinal Substrates

Luiz Enger, Stéphane Flament, Imtiaz Bhatti, Olivier Rousseau, Bruno Guillet, Marc Lam Chok Sing, Victor Pierron, Sylvain Lebargy, Sandeep Chaluvadi, Bernadette Domengés, et al.

▶ **To cite this version:**

Luiz Enger, Stéphane Flament, Imtiaz Bhatti, Olivier Rousseau, Bruno Guillet, et al.. Key Parameters for Detectivity Improvement of Low Noise Anisotropic Magnetoresistive Sensors Made of La 2/3 Sr 1/3 MnO 3 Single Layers on Vicinal Substrates. ACS Applied Electronic Materials, 2023, 5 (2), pp.729-739. 10.1021/acsaelm.2c01096 . hal-04107995

HAL Id: hal-04107995
https://hal.science/hal-04107995

Submitted on 26 May 2023

HAL is a multi-disciplinary open access archive for the deposit and dissemination of scientific research documents, whether they are published or not. The documents may come from teaching and research institutions in France or abroad, or from public or private research centers.

L'archive ouverte pluridisciplinaire **HAL**, est destinée au dépôt et à la diffusion de documents scientifiques de niveau recherche, publiés ou non, émanant des établissements d'enseignement et de recherche français ou étrangers, des laboratoires publics ou privés.

Key parameters for detectivity improvement of low noise anisotropic magnetoresistive sensors made of $La_{2/3}Sr_{1/3}MnO_3$ single layers on vicinal substrates

Luiz G. Enger,[†] Stéphane Flament,[*,†] Imtiaz N. Bhatti,[†] Olivier Rousseau,[†] Bruno Guillet,[†] Marc Lam Chok Sing,[†] Victor Pierron,[†] Sylvain Lebargy,[†] Sandeep K. Chaluvadi,[†] Bernadette Domengès,[‡] Arturo Vera,[¶] Jose M. Díez,[§] Isidoro Martínez,[¶,‖] Ruben Guerrero,[¶] Lucas Pérez,[¶,⊥] Maria T. Gonzalez,[¶] Rodolfo Miranda,[¶,§] Julio Camarero,[¶,§] Paolo Perna,[¶] and Laurence Méchin[†]

†*Normandie University, UNICAEN, ENSICAEN, CNRS GREYC, 14000 Caen, France*

‡*Normandie University, UNICAEN, ENSICAEN, CNRS CRISMAT, 14000 Caen, France*

¶*IMDEA Nanociencia, Campus de Cantoblanco, 28049 Madrid, Spain*

§*Dept. Física de la Materia Condensada, INC and IFIMAC, Universidad Autónoma de Madrid, 28049 Madrid, Spain*

‖*Faculty of Experimental Sciences, Universidad Francisco de Vitoria, Pozuelo de Alarcón, Madrid, 28223, Spain*

⊥*Dept. Fisica de Materiales, Universidad Complutense de Madrid, 28040 Madrid, Spain*

E-mail: sflament@ensicaen.fr

Abstract

The current trend in magnetoresistive sensors development is to increase the sensitivity of single sensing elements by using multilayer structures and to design them into arrays. Such arrays are designed to compensate the excess low frequency noise of individual elements, which limits their magnetic resolution. Here, we report the modeling, design and fabrication of single layer anisotropic magnetoresistive (AMR) sensors using low noise epitaxial $La_{2/3}Sr_{1/3}MnO_3$ (LSMO) oxide thin films deposited on vicinal $SrTiO_3$ substrates. The fabrication process is simple and the operation of the sensor is based on a step-induced uniaxial magnetic anisotropy, described using the Stoner-Wohlfarth model. A coherent magnetization reversal process is observed by magneto-optical Kerr effect imaging. A good agreement between experimental data and the expected sensor response confirms the correct operation of the device. Three main fabrication parameters, namely the vicinal angle of the substrate, the deposition temperature, the thin film thickness, and their effects on film anisotropy field and device detectivity have been studied. Detectivity levels as low as 1.4 nT $Hz^{-1/2}$ at 1 Hz and 240 pT $Hz^{-1/2}$ in white noise region are achieved with a single Wheatstone bridge element operating at 310 K. Compared to GMR and AMR sensors, these results are promising for further development and for their use as single layer LSMO low-field AMR sensors, including applications as implantable biomedical devices.

Keywords

magnetic sensor, anisotropic magnetoresistance, manganite, thin film, vicinal substrate

1 Introduction

The technological progress in the past few years has allowed the fabrication of low cost, low power consumption and high sensitivity magnetoresistive sensors . They are used in a wide range of applications for the automotive industry, non-destructive monitoring, wearable electronics, position sensing and biomagnetism.[1] If biomedical applications are targeted, the sensor should present a high signal-to-noise ratio in the low frequency region, as biological signals typically operate below

1 kHz.[2–4] Currently, superconducting quantum interference devices are mainly used for detecting magnetic signals of the human body.[5,6] While they are able to detect ultra-low magnetic fields, they operate at cryogenic temperatures, which requires them to be placed at a minimum distance from the source of the signal to be detected (and also needs infrastructure). Recently, optically pumped magnetometers have been used as an alternative,[4,7] but they need to operate in magnetically shielded room and cannot be implanted in the body for long time recording. Placing the sensor as close as possible to the source of the signal is a key point for improving the signal to noise ratio. So, if the device has to be implanted, an optimal operation at body temperature and a small size are required, both for local analysis and for design of small gradiometric structures which can avoid the use of shielded rooms. Although giant magnetoresistance (GMR)[8,9] and tunneling magnetoresistance (TMR)[10,11] sensors present a high sensitivity, their complex multilayer structure generates significant intrinsic excess noise at low frequency.[12] Complex architectures of stacked spin valves or magnetic tunnel junctions connected in series and in parallel are required to reach sub-nT resolutions[13–15] . Sub-nT resolution can also be obtained with multilayer AMR based sensor.[16] By exploiting the very low intrinsic noise and the AMR effect in ferromagnetic $La_{2/3}Sr_{1/3}MnO_3$ (LSMO) oxide thin films, we have fabricated magnetoresistive sensors, with a single ferromagnetic layer structure, targeting performance adapted to biomedical applications. These AMR sensors have a Wheatstone bridge geometry similar to Planar Hall Effect Bridges (PHEB).[17] We did not rely on exchange bias interaction with a pinned layer nor on the application of external magnetic field during deposition process, which is commonly the case for GMR, TMR and PHEB devices. In our case, the uniaxial magnetic anisotropy was set and imposed by the vicinal $SrTiO_3$ (STO) substrate.[18,19] Thus, there is no magnetic or transport noise due to interaction between different magnetic layers. This allows a much simpler fabrication process and the sensing element can be scaled easily with a flexible design. In this paper the principle of operation of such an AMR sensor is presented with attention given to magnetic energy states. Expressions of magnetic sensitivity and detectivity are given. The model is validated via Magneto-optical Kerr Effect (MOKE) imaging and magnetoresistance characterization of sensors. Three parameters were stud-

ied to tune the anisotropy field of the LSMO thin film and thus improve the sensor performance: the vicinal angle of the substrate, the temperature during epitaxial deposition of the film and the thin film thickness. A comparison with GMR and TMR structures in terms of size, detectivity and power consumption is provided which shows that our sensors are quite competitive. A sub-nT resolution is achieved at 310 K temperature for the best samples. Such performance are compatible with the requirements of biomedical applications and show that AMR sensors based on LSMO are viable candidates for biomedical applications.

2 Experimental Section

2.1 Sensor Fabrication.

The vicinal $SrTiO_3$ substrates were acquired from Crystal GmbH, in rectangular shape of 5 mm by 10 mm, with a 0.5 mm thickness. The LSMO target was obtained from SurfaceNet GmbH. Thin film deposition was performed using a Pulsed Laser Deposition (PLD) system supplied by Twente Solid State Technology company (https://www.tsstsystems.com/), equipped with a Reflection High-Energy Electron Diffraction (RHEED) which allows to monitor the growth of monolayers. During deposition, the STO substrate is heated with a 980 nm infrared laser. A KrF laser with 248 nm wavelength is fired at the LSMO target. The spot energy was 1.7 J cm^2 over a 1.5 mm by 1.4 mm area and the firing rate was 3 Hz. The chamber was kept at 0.2 mbar 0_2 pressure. *In-situ* deposition of Au is performed at 5 Hz firing rate, and the gold layer was then made thicker with Ion Gun Evaporation by GATAN. A two-steps standard photolithography process defined the gold pads and Wheatstone bridge. Gold was etched in a KI solution, whereas LSMO was etched using Ion Beam Etching with Ar ions.

2.2 Magnetic Characterization.

A longitudinal Magneto-optical Kerr Effect (MOKE) system developed in-house was used for magnetic characterization of etched LSMO samples. The system uses a high power LE B P1W-EZFZ-24 LED from OSRAM Opto Semiconductors at 459 nm, powered by a SIGLENT SPD1168X Programmable DC Power Supply. Reflected light is captured using a Hamamatsu ORCA-Flash 2.8 Scientific CMOS camera. A pair of Helmholtz coils with soft a ferrite core creates the required magnetic field using a SIGLENT SPD3303X Programmable DC Power Supply. The coils were calibrated using a commercial Hall effect sensor.

2.3 Electrical Characterization.

For magnetoresistance and noise characterizations, the samples were placed into a LakeShore Model EMPX-HF probe station. Temperature is controlled by a LakeShore Model 336 Temperature Controller. The Sensor is voltage biased with a Yokogawa GS200 DC Voltage/Current Source, and the applied magnetic field is swept while the voltage across the Wheatstone bridge is measured with a Keythley 2000 Multimeter after amplification using a lab-made preamplifier, adapted to our sample characteristics. Noise measurements are performed with a Hewlett-Packard 3562A Dynamic Signal Analyzer.

3 Results and Discussion

3.1 Principle of Operation and Modeling

3.1.1 Device geometry and principle of operation

Figure 1 presents a schematic view of the sensor showing relevant physical parameters and directions of interest. The sensor consists of a full Wheatstone bridge structure patterned in an epitaxial

LSMO thin film which is ferromagnetic below its Curie temperature.[20] Epitaxial deposition was performed on vicinal STO substrate (Figure 1a), presenting a surface with respect to the crystallographic plane, forming a structure with steps and terraces. An easy magnetic axis is induced along the step edges.[21–23] Figure 1b shows a scanning transmission electron microscopy (STEM) view of the interface. It confirms that LSMO grows with its (001) crystallographic axis parallel to the (001) axis of the STO. We consider that each arm of the Wheatstone bridge behaves like a single in-plane magnetic domain and we define θ as the angle between the asy magnetization axis and magnetization M.

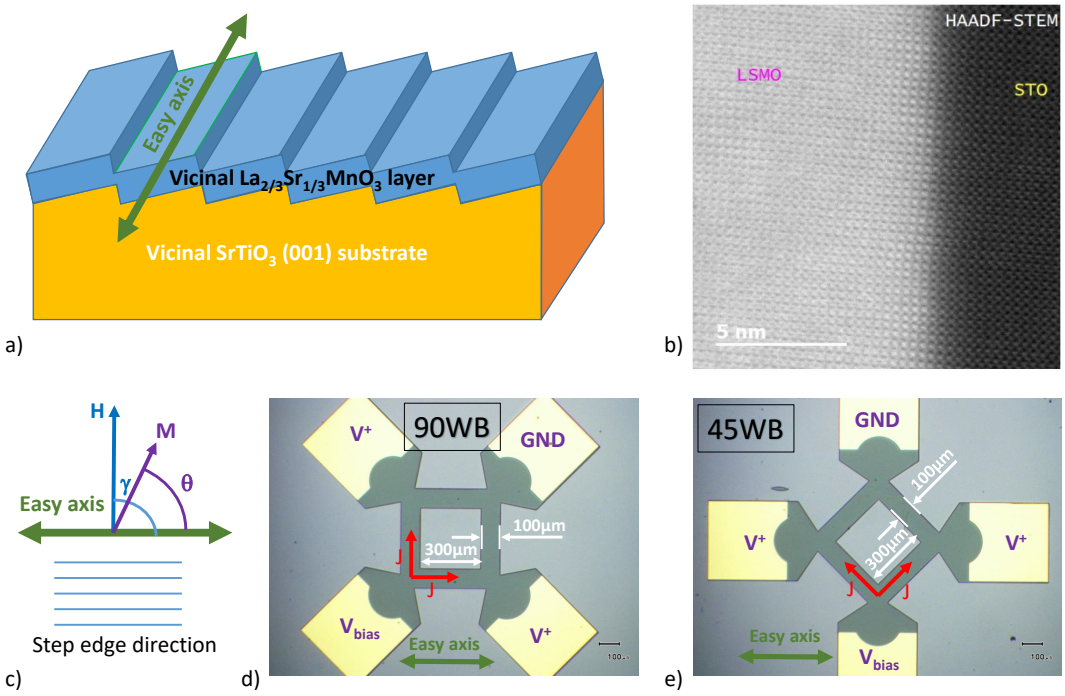

Figure 1. Representation of the LSMO device. a) schematic view of the vicinal LSMO layer deposited on a vicinal STO substrate. The easy magnetic axis (green arrow) is parallel to step edges. b) STEM view of the epitaxial growth of the LSMO layer on the STO substrate. c) Magnetic field H (blue) applied in the plane of the LSMO films at an angle γ to the easy axis and magnetization M settled in the plane of the LSMO layer at an angle θ to the easy axis. d) 90WB Wheatstone bridge design etched in the LSMO layer including gold pads (yellow). The direction for current density in the arms (red) is either parallel or perpendicular to the easy axis. e) 45WB Wheatstone bridge design. The direction for current density in the arms (red) is at 45° or 135° to the easy axis.

Due to the AMR effect, the electrical resistance of each arm depends on the angle between magnetization and current density directions. The current direction is fixed by the arm geometry

and thus the angle α between the easy axis and current density J can be fixed on purpose by the design (Figure 1c). Wheatstone bridges were etched so that the arms present α values equal to either 0° or 90° (90WB design) or α values equal to either 45° or 135° (45WB design) as depicted in Figures 1d and 1e.

A current density J will create an electric field E through the resistivity tensor ρ, following the expression $E = [\rho]J$. The resistivity tensor is given by

$$\rho = \begin{bmatrix} \rho_\perp - \Delta\rho \cdot \cos^2\theta & -\frac{1}{2}\Delta\rho' \cdot \sin(2\theta) \\ -\frac{1}{2}\Delta\rho' \cdot \sin(2\theta) & \rho_\perp - \Delta\rho \cdot \sin^2\theta \end{bmatrix} \tag{1}$$

where $\Delta\rho = \rho_\perp - \rho_\parallel$, $\rho_\perp$ is the resistivity when magnetization is perpendicular to the easy axis and $\rho_\parallel$ is the resistivity when magnetization is parallel to said axis. We consider the X-axis to be the easy magnetization axis of the single domain. In the present work, $\Delta\rho$ was defined as such to have a positive value. We also define ρ_0 as the mean resistivity value, $\rho_0 = (\rho_\parallel + \rho_\perp)/2$. The main diagonal terms correspond to the usual AMR effect and the antidiagonal terms correspond to the *planar Hall effect* (PHE).[24,25] The latter induces a voltage difference transversal to the passing current, similar to the usual Hall effect when a magnetic field is applied perpendicular to the sample plane. The use of $\Delta\rho'$ is to account for possible differences in resistivity variations between AMR and PHE. Resistivity and its variations can present different values depending on the direction of applied current, according to the crystalline structure of the material. From now on, electrical resistance of the etched film will be used instead of resistivity. Therefore, we can define ΔR, $\Delta R'$ and R_0 similarly as $\Delta\rho$, $\Delta\rho'$ and ρ_0. Arms at a 90° angle to each other present opposite signs of electrical resistance variations for the same change in θ angle.[26] Considering that the four arms present the same values for ΔR (respectively $\Delta R'$) and R_0, the output signal can then be written for the 90WB (respectively 45WB) design as

$$V_{meas}^{90WB} = V_{bias}\left(\frac{\Delta R}{2R_0} - \frac{\Delta R}{R_0}\sin^2\theta\right) \tag{2}$$

$$V_{meas}^{45WB} = V_{bias}\frac{\Delta R'}{R_0}\sin 2\theta \tag{3}$$

where V_{bias} is the bias voltage of the Wheatstone bridge.

In single magnetic domain approximation, we take into account the uniaxial magnetic anisotropy energy and the magnetic field energy only. Using Stoner-Wohlfarth model, the angle θ at equilibrium can be obtained by minimizing the following dimensionless magnetic energy density[27]

$$\frac{E}{2K_u} = \frac{1}{2}\sin^2\theta - \frac{H}{H_a}\cos(\theta - \gamma) \tag{4}$$

Here, γ is the angle between easy magnetization axis and applied field H, $H_a = 2K_u/(\mu_0 M_S)$ is the anisotropy field, K_u the uniaxial anisotropy constant and M_S the saturated magnetization. When the magnetic field is applied perpendicular to the easy axis, $\gamma = 90\ ^\circ$ and a analytical expression for magnetization direction at equilibrium can be written as

$$\theta_{eq} = \arcsin\left(\frac{H}{H_a}\right) \tag{5}$$

When substituting it in Equation (2), we can re-write the voltage output for 90WB and 45WB devices as

$$V_{meas}^{90WB} = V_{bias}\frac{\Delta R}{R_0}\left(\frac{1}{2} - \frac{H^2}{H_a^2}\right) \tag{6}$$

$$V_{meas}^{45WB} = V_{bias}\frac{\Delta R'}{R_0}\frac{H}{H_a}\sqrt{1 - \frac{H^2}{H_a^2}} \tag{7}$$

which are valid for $|H| \leq H_a$. We deduce from these expressions that for 90WB design, the Full Width at Half Maximum (FWHM) of the V_{meas}^{90WB} curve is equal to $\sqrt{2}H_a$. To obtain the widest linear range of operation and have an easier comparison parameter, in this work we will operate at a bias field of $H = -H_a/2$ for this design. For 45WB design, the V_{meas}^{45WB} curve is linear around zero field and the total width between extrema values is equal to $\sqrt{2}H_a$.

3.1.2 Sensitivity, noise and detectivity

From equations (6), the expression of sensitivity S for 90WB design at a bias field of $H = -H_a/2$ is calculated as

$$S = \frac{\partial V_{meas}}{\partial \mu_0 H} = V_{bias} \frac{\Delta R}{R_0} \frac{1}{\mu_0 H_a} \tag{8}$$

In the case of the 45WB design, from equation (7), the same expression is obtained at zero field bias, provided ΔR is replaced by $\Delta R'$. Higher sensitivity is obtained with high MR ratio, defined as $\Delta R/R_0$ (respectively $\Delta R'/R_0$), and low anisotropy field H_a. The detectivity of a sensor is defined as the ratio of the noise voltage spectral density by the device sensitivity. For a magnetic sensor it represents the smallest magnetic field that can be detected at a given frequency. Therefore to be able to detect weak magnetic signals, a low intrinsic electrical noise is also required. Previous studies[28–30] have shown that LSMO thin films present thermally induced Johnson-Nyquist[31,32] white noise and a very low excess noise in the low frequency region that can be described by the phenomenological Hooge expression,[33] also used to describe the excess noise in other magnetoresistive devices.[34] For a Wheatstone bridge patterned in a LSMO layer with four arms of the same volume Ω and the same electrical resistance R, the total noise spectrum S_V can be expressed as the sum of low frequency excess noise and thermal noise as

$$S_V = \sqrt{\frac{\alpha_H}{n} \frac{1}{f\Omega} \frac{V_{bias}^2}{4} + 4k_B T R} \tag{9}$$

where α_H/n is the normalized Hooge parameter, which is intrinsic to the resistor element material, f is the observed frequency, V_{bias} is the bias voltage, k_B is the Boltzmann's constant and T is the operating temperature. Assuming a readout electronics with a noise much smaller than the noise of the sensor, the detectivity $D = S_V/S$ of the 90WB device can finally be written as

$$D = \mu_0 H_a \frac{R_0}{\Delta R} \sqrt{\frac{\alpha_H}{n} \frac{1}{4\Omega f} + \frac{4k_B T R}{V_{bias}^2}} \tag{10}$$

Again, the same expression is obtained for the 45WB design just by replacing ΔR by $\Delta R'$. This equation can be used as a guide on how to obtain lower detectivity values (in other words, better performance) by varying one of its parameters. Increasing the bridge voltage bias or reducing the electrical resistance will improve the detectivity in the thermal noise region while keeping unchanged the detectivity in the low frequency region. In the low frequency domain, the detectivity will be improved by increasing the volume or by using a material with reduced normalized Hooge parameter, which will not change the detectivity in the thermal noise domain. For low frequency applications, a material with very low α_H/n is attractive. With MR ratio and α_H/n related to the material itself, an actual tunable parameter to improve performance is the anisotropy field H_a. Different strategies were investigated to lower H_a and thus improve the detectivity in both low frequency and white noise regions.

3.1.3 Validation of uniaxial magnetic anisotropy induction

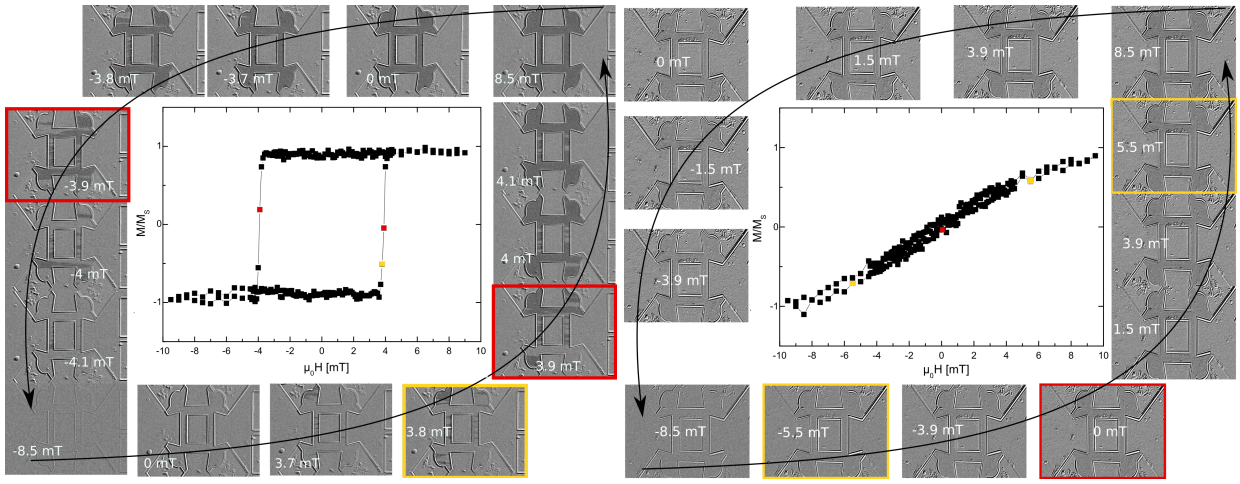

(a) **(b)**

Figure 2. Longitudinal MOKE imaging at room temperature and deduced magnetization loop when magnetic field is applied horizontally along the a) easy axis and b) hard axis. Sample is a 60 nm thick LSMO film deposited on 8° vicinal STO at 730 °C.

To validate the correct operation of single layer AMR sensors, first we fabricated samples consisting of 60 nm thick LSMO thin films deposited by Pulsed Laser Deposition (PLD) technique over 4° or 8° vicinal STO and ion beam etched them into a Wheatstone bridge geometry after

standard UV lithography. As it was reported earlier by the authors,[19] uniaxial magnetic anisotropy can be induced in LSMO thin films when epitaxial deposition is performed on vicinal substrates using PLD. In our case, we opted for 4° or 8° vicinal STO to achieve the desired uniaxiality.[18,19] In this section, experimental data supporting the physical model are for 8° vicinal STO samples which present a stronger uniaxial anisotropy; similar results were obtained on 4° vicinal STO samples. In Section 3.2, results obtained using 4° or 8° vicinal STO will be compared. The uniaxial magnetic anisotropy was checked using a homemade longitudinal Magneto-optical Kerr Effect (MOKE) setup that provides the component of the in-plane magnetization in the direction of the magnetic field. Due to the very small Kerr effect in LSMO thin films, a differential technique was used. All images acquired during the magnetization cycle, from one saturated state to the other and then backwards, are subtracted from a reference image corresponding to an initial saturated state. Final images are in gray levels, and the darker the area the larger is the magnetization component opposite to the initial saturated state. It is thus possible to deduce from these images the magnetization cycle in any arm of the Wheatstone bridge[35] as shown in Figure 2. Magnetization cycles are surrounded with selected MOKE images of the sample obtained at discrete magnetic field values. The bottom-left corner presents the image at negative field saturation, which is also the reference image used to enhance contrast. The top-right corner presents the sample at positive field saturation, with the magnetic material appearing at its darkest gray level. The black arrows indicate the direction of field sweep and some specific points in the cycle are highlighted to indicate the respective original image. When the magnetic field is applied parallel to the easy axis, we observe nucleation and then propagation of domains and a square shaped hysteretic magnetization loop is obtained. When the field is applied perpendicular to the easy axis, a coherent magnetization reversal process is observed and the magnetization loop is linear between saturated states and has no hysteresis.

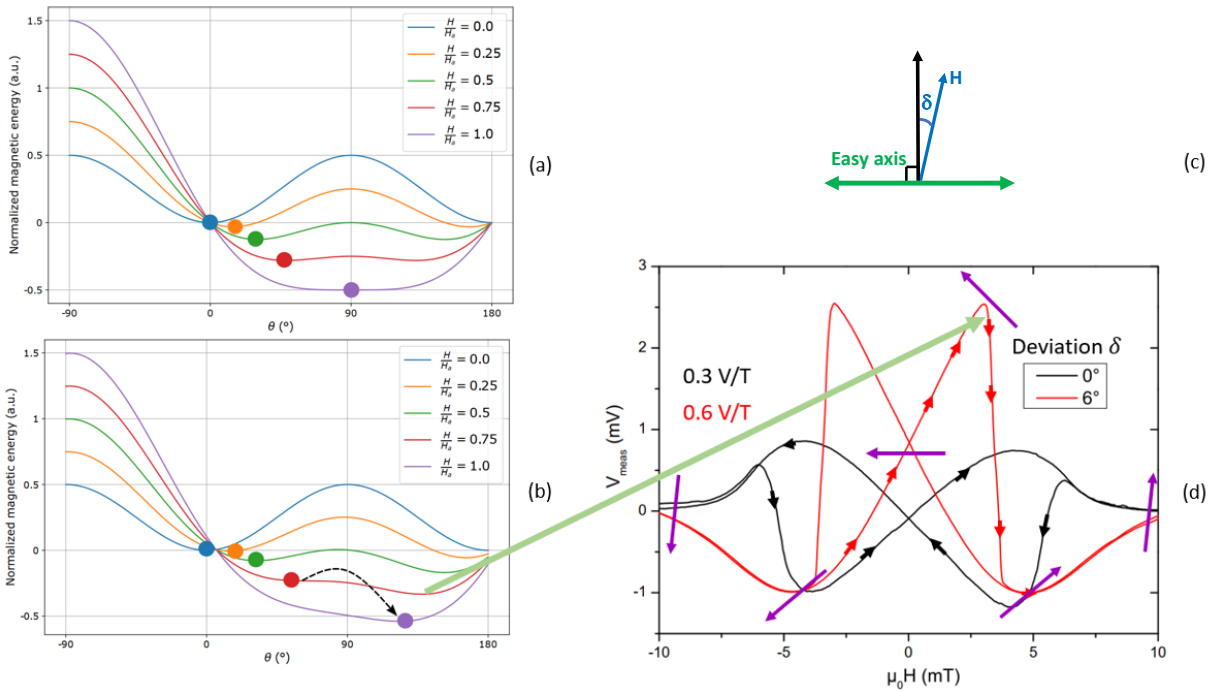

Figure 3. Dimensionless magnetic energy versus θ for increasing H/H_a ratio when a) $\delta = 0°$ and b) $\delta = 6°$. Dots represent the energy minimum at equilibrium, and dashed arrow indicates the jump in magnetization direction. c) Applied field with a small deviation δ from normal direction to easy axis. d)Experimental voltage output of a 45WB device when $\delta = 0°$ (black curve) and when $\delta = 6°$ (red curve). Violet arrows indicate the magnetization direction. The green arrow from b) to c) points out the sudden variation in V_{meas} due to the magnetization jump.

3.1.4 Control of coherent and constructive rotation of magnetization

When the field is applied perfectly normal to the easy axis ie when $\gamma = 90°$, from an initial saturated state normal to the easy axis ie when $\theta_{eq} = -90°$, the direction of rotation from one saturated state to the other can be either clockwise or counter-clockwise. Even though a coherent magnetization rotation is observed in all arms, the direction of rotation in each arm is free indeed and may thus not be the same over the whole structure. As the MOKE imaging system provides the relative magnitude of magnetization along applied field but not its direction, it is not possible to assess that magnetization does rotate in the same direction over the whole bridge, which is required for a correct operation of the sensor and for getting the maximum output voltage. To ensure the same rotation in all arms, magnetoresistance measurements have been performed with the magnetic field applied not exactly perpendicular to the easy axis but at an angle $\gamma = 90° - \delta$. The small deviation

δ of a few degrees gives rise to a weak component of the applied field along one specific direction of the easy axis, which forces a common direction for magnetization rotation in all arms of the Wheatstone bridge. Considering an initial saturated state with $\theta_{eq} = -90°$ (corresponding to a negative applied field strong enough to saturate the film), we plot in Figure 3 the dimensionless magnetic energy defined in Equation (4), as a function of θ, for different positive values of the applied field H. When δ is null (no deviation), two energy minima symetrically apart with respect to $\theta = 90°$ are present. Considering that θ increases continuously from $\theta = -90°$ as H is increased, the θ_{eq} value for θ at equilibrium corresponds to the smallest value of θ for which the energy is minimum. These are pointed by dots in Figure 3a and always occur at $\theta < 90°$. The energy barrier between the two energy minima continuously decreases as H is increased and for $H = H_a$ the magnetization becomes parallel to H, since the energy minimum corresponds to $\theta = 90°$. When a small deviation δ is introduced, the energy curve gets deformed. Energy minima are still well separated on both sides of a vertical axis located at $\theta = 90°$, but no longer at the same energy level. In addition to this, for an increasing field the energy barrier vanishes before H reaches H_a, as can be observed in Figure 3b. Thus, as long as the applied field is less than the critical value for which the energy barrier disappears, θ_{eq} at equilibrium is less than 90°. When H rises slightly above this critical value, the magnetization direction undergoes a sudden jump, since the energy minimum corresponds to a θ_{eq} value higher than 90°. The main effect of this magnetization switch is a sudden variation in voltage output V_{meas}, as shown in Figure 3 on a 45WB sample. After the jump, there is a continuous decrease of θ_{eq} down to 90° as the field is increased. It has to be noted that the field required to achieve magnetization parallel to H is in this case much larger than H_a and as a consequence, the AMR curves present smoothly curved extremities around $-H_a$ and $+H_a$. For sensor operation, the sudden variation in voltage output V_{meas} is not a problem as it occurs outside the operation range of the device.

When δ is non zero, it is no longer possible to write an analytical expression for θ_{eq} as expressed by Equation (5) and neither can we calculate the anisotropy field from the FWHM of the $V_{meas}(H)$ curve. It is nevertheless possible to evaluate H_a from a numerical model to fit Equation

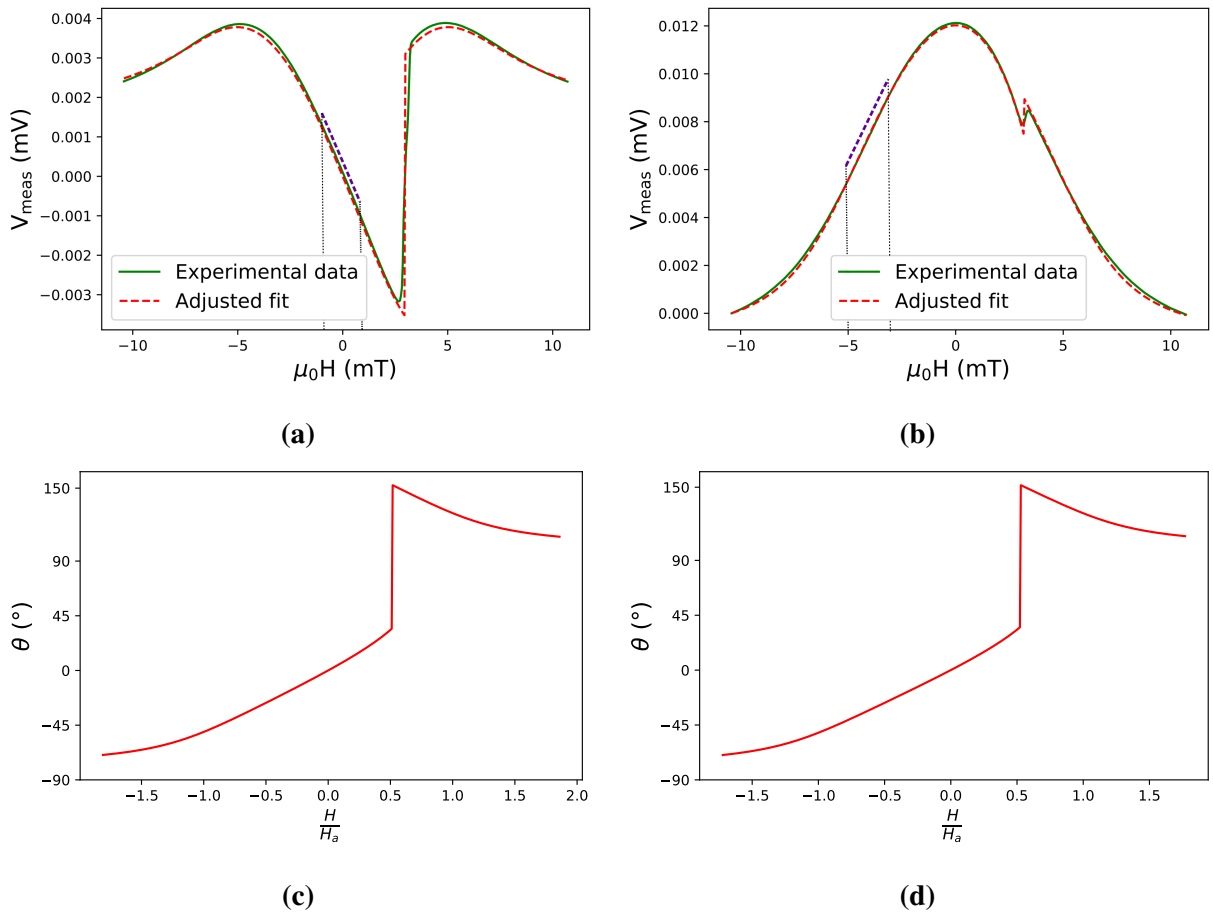

Figure 4. Experimental AMR curves from 8° vicinal sample for a) 45WB and b) 90WB devices. Using Eq. (3) and Eq. (2) , the calculated $V(H)$ is superimposed on the experimental $V_{meas}(H)$ data. The linear operating range of both 45WB and 90WB are indicated with purple dashed lines. By minimizing the right hand side of Eq. (4), θ values are obtained for c) 45WB and d) 90WB.

(2) over experimental data. Starting with a given range for H_a, $\Delta R/R_0$ and δ parameters, this fit is performed by obtaining θ_{eq} from a numerical minimization of Equation (4). Parameters are optimized in order to reduce the global error between the experimental data and calculated curve. A good agreement between the numerical fit and experimental data, as displayed in Figure 4, shows that our sample presents the expected magnetic behavior and which allows the extraction of the anisotropy field value H_a. The anisotropy field value H_a deduced from the fit is 5.8 mT for 45WB and 6.0 mT for 90WB.

3.2 Performance improvement by reducing the anisotropy field

Keeping unchanged the geometry of the 90WB Wheatstone bridge, three fabrication parameters were varied to study their effect on anisotropy field: vicinal angle of the substrate, substrate temperature during PLD and LSMO thin film thickness. All electrical measurements were performed at the same 5 V bias voltage and at 37 °C sample temperature, in order to compare $V_{meas}(H)$ and electrical noise. The electrical noise of the devices were measured using a homemade low noise amplifier.[36] Experimental curves of $V_{meas}(H)$ were shifted to set the minimum value to zero. The same investigations were performed and the same conclusions were obtained for both 90WB and 45WB designs. As we systematically verified a $\Delta R'$ lower than ΔR, only data from the 90WB design are presented.

3.2.1 Effect of substrate vicinal angle and deposition temperature

According to the expression $H_a = 2K_u/(\mu_0 M_S)$, a reduction in K_u and an increase in M_S should result in a smaller anisotropy field, and thus a lower detectivity. To study this effect in our sensors, we fabricated 60 nm thick samples over 4° and 8° vicinal substrates with a parallel investigation of STO substrate temperature during PLD. The miscut angle present in vicinal substrates is directly linked to the anisotropy constant K_u.[18] Substrates with higher vicinal angle have reduced terrace width which increases the uniaxial anisotropy contribution.[21] A 730 °C substrate temperature was found to be the optimal condition for high crystalline quality of LSMO thin film deposited via PLD. Thus, performing deposition at lower temperature may reduce film's Curie temperature T_C due to lower film quality. As the temperature was fixed at 37 °C for electrical characterization, a lower T_C means a lower value of M_S at 37 °C. It is thus expected to observe a reduction of the anisotropy field, since H_a is proportional to M_S^p with p strictly positive.[37,38] For 4° and 8° vicinal STO, samples were prepared at 730 °C and 680 °C, and an additional 630 °C deposition temperature was also investigated for 8° vicinal STO. Magnetoresistance characterization of all 60 nm thick samples is presented in Figure 5. The sensitivity values were obtained from the numerical derivative of the experimental $V_{meas}(H)$ curves. The dashed lines with open symbols is the calcu-

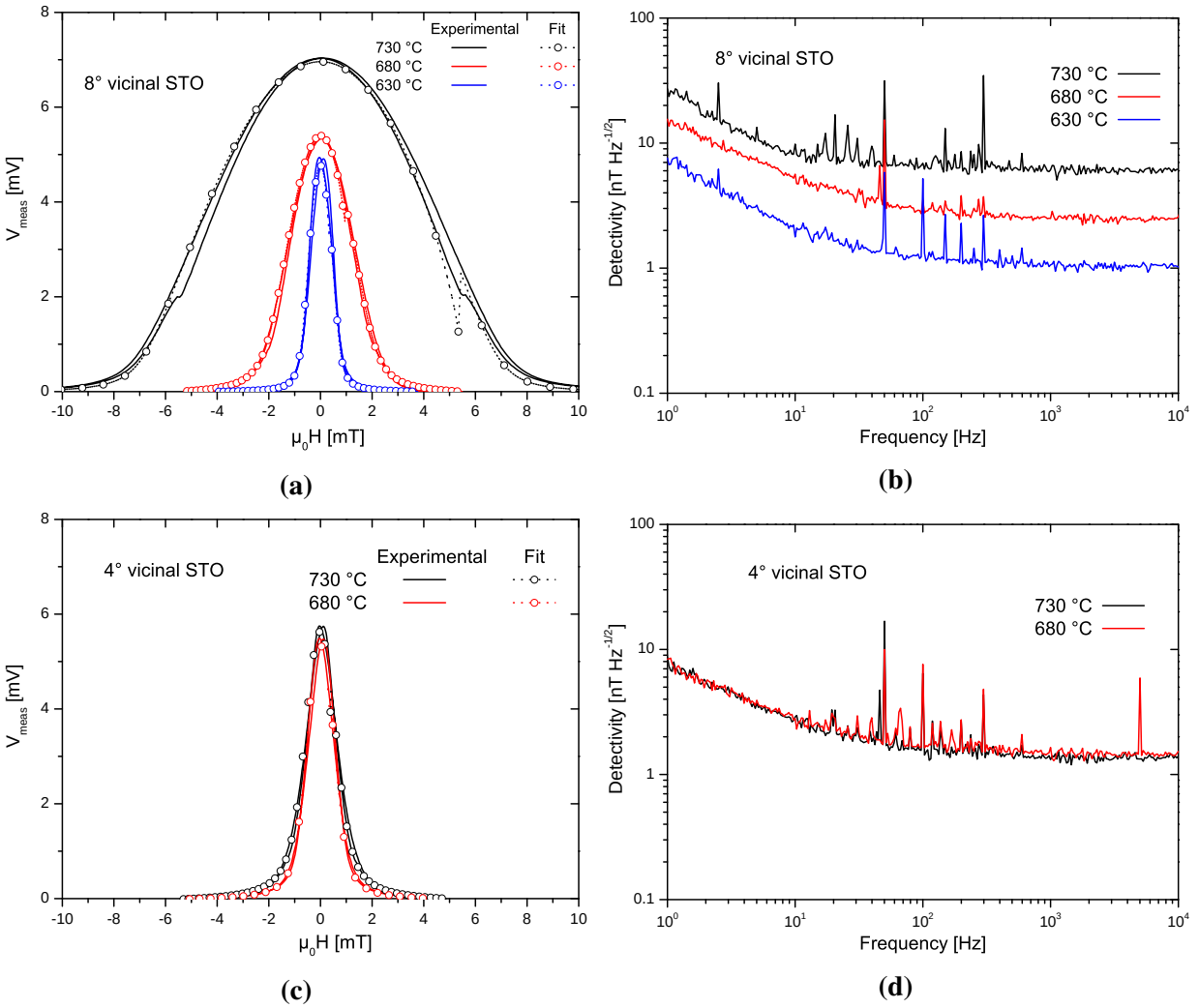

Figure 5. Effects of substrate vicinal angle and deposition temperature in 60 nm films. Experimental shifted $V_{meas}(H)$ curves and numerical fit derived from energy minimization for a) 8° and c) 4° vicinal substrates. Detectivity deduced from measured noise and sensitivity at 5V bias for b) 8° and d) 4° vicinal substrates.

lated V_{meas}, obtained from the numerical energy minimization scheme. For this calculated V_{meas} only the curve from negative to positive magnetic field is represented. The effect of vicinal angle and deposition temperature on H_a can also be verified by the FWHM of experimental $V_{meas}(H)$ curves, and are presented in Table 1. They do present a good agreement with the value obtained by curve fitting, confirming the possibility to use this method for H_a estimation. As the anisotropy field is reduced, saturation is reached for a lower applied field. For 8° vicinal STO, a clear reduction of H_a can be seen when the deposition temperature is decreased, as expected. Although MR

ratio also decreased, it had a lower effect on sensitivity. Samples present similar noise values, so that the best performance is finally achieved with 630 °C deposition temperature. In the case of 4° vicinal STO, reducing the temperature had minor effects on MR. It had also a minor effect on anisotropy field, which requires further investigation for proper explanation. This led to a similar performance for both samples. To conclude, comparable performance could be achieved with either 8° or 4° vicinal STO substrates. A considerable reduction in H_a is obtained when reducing the vicinal angle, and although a significant change in noise was not verified with lower temperatures during PLD, it is preferable to use optimized deposition parameters for reproductibility. For these optimized deposition parameters the 4° vicinal samples had a detectivity almost five times better than the 8° ones, therefore we opted to keep the 4° vicinal substrate for the investigation on thin film thickness.

3.2.2 Effect of thin film thickness

Samples with 60 nm, 45 nm and 30 nm thick LSMO were investigated. 4° vicinal STO substrates were used to sett small values of H_a and film deposition was performed at the optimum temperature of 730 °C. Voltage output and detectivity results are presented in Figure 6. Samples presented an

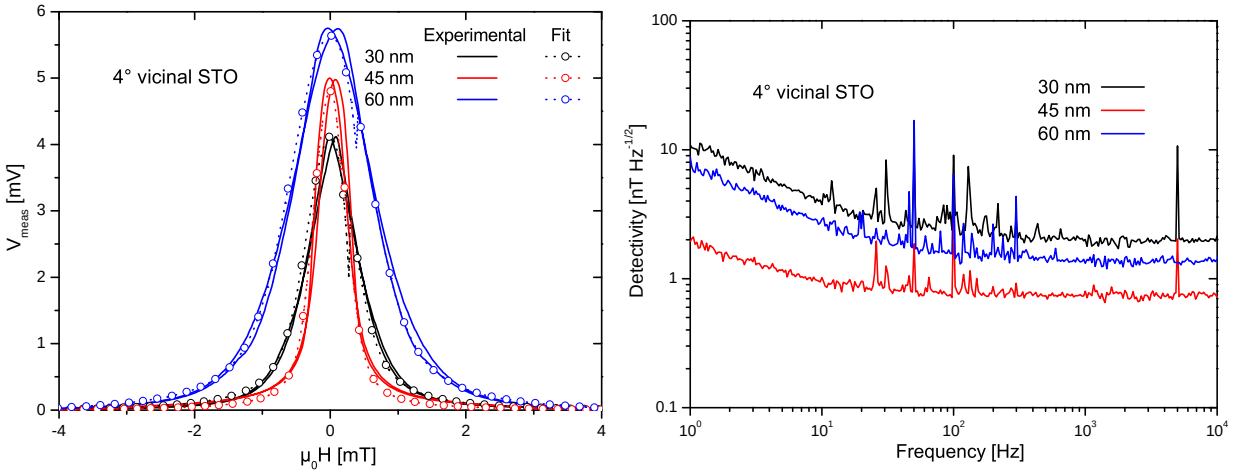

Figure 6. Characterization of samples on 4° vicinal STO and 730 °C deposition temperature. a) $V_{meas}(H)$ curves for different film thickness and b) corresponding detectivity, measured at 5 V bias.

increase in MR ratio as the thickness increased (Figure 6). But, whereas 30 nm and 45 nm thick samples have a similar value of H_a, the 60 nm film presents the largest anisotropy field. This can be explained by the fact that when thickness increases the step-induced uniaxial anisotropy is reduced, and the device no longer behaves as desired. In the case of LSMO films deposited on non-vicinal (flat) STO substrates, the uniaxial anisotropy obtained for low thickness films (typically 12 nm) turns to a biaxial anisotropy for 50 nm thick films, with a coercivity in the easy axis direction larger than for the 12 nm thick films.[39] A similar loss of uniaxial anisotropy may also occur in thicker LSMO films deposited on vicinal substrates.

In this work, in the case of films deposited on 4° vicinal substrate, a clear uniaxial anisotropy is observed for 30 and 45 nm thick films with fully reversible hard axis magnetization loop (not shown). For 60 nm thick films, if a clear unixial anisotropy was observed when films were deposited on 8° vicinal substrate, some hysteresis was observed when films were deposited on 4° vicinal substrate, revealing a growing biaxial anisotropy contribution. For reducing the noise, the thicker the film the better are the performance. The thickness has nevertheless to be limited to a value that will maintain the anisotropy field low and the anisotropy uniaxial. The smallest anisotropy field was obtained for the thickness intermediate value of 45 nm, resulting in the highest sensitivity. As seen in Figure 6b, this sample presented the lowest detectivity of this set. Despite presenting the smallest sensitivity of this set, the 60 nm thick sample presented a better performance than the 30 nm thick one thanks to lower intrinsic noise. In Table 1 a summary of results obtained from all samples is presented, and the improvement of sensor performance by anisotropy field reduction is clearly seen. The best performance is obtained for 45 nm LSMO deposited at 730 °C on 4° vicinal substrate.

3.2.3 Effect of bias voltage

Considering the resilience to deposition temperature change of films deposited on 4° vicinal STO and the best detectivity obtained for 45 nm film thickness, a deeper analysis of 45 nm thick LSMO over 4° vicinal STO sample was performed by changing the voltage bias of the Wheatstone bridge.

Table 1. Evolution of anisotropy field and performance of the Wheatstone bridge LSMO AMR sensor.

Substrate	8° vicinal			4° vicinal		
Deposition temperature	730 °C	680 °C	630 °C	730 °C	730 °C	730 °C
Thin film thickness	60 nm	60 nm	60 nm	60 nm	45 nm	30 nm
$\mu_0 H_a$ [mT] from FWHM	6.6	2.0	0.6	0.9	0.3	0.5
$\mu_0 H_a$ [mT] from $V_{meas}(H)$ fit	6.4	1.8	0.7	0.8	0.3	0.5
S [% T^{-1}]	26	62	155	111	283	111
D [nT Hz$^{-1/2}$] at 1 Hz	27.0	15.0	7.6	8.7	1.9	11.0
D [nT Hz$^{-1/2}$] at 1 kHz	6.1	2.5	1.1	1.3	0.8	2.0

This allow us to verify the evolution of sensitivity, noise and detectivity. Characterization curves of this sample are presented in Figure 7.

We checked that uniaxial anisotropy and coherent magnetization reversal were maintained. Electrical noise in low frequency region increases with voltage bias as predicted by Equation (9), while broadband noise is limited by device resistance. Knowing the volume $\Omega = 1.35 \times 10^{-15}$ m^3 and the measurement temperature $T = 310$ K, the fit over measured noise was obtained with $\alpha_H/n = 1.2 \times 10^{-31}$ m^3 and $R = 5.5$ kΩ. Such a low α_H/n value of 10^{-31} m^3 is typical for high quality epitaxial LSMO films.[29] The good agreement between measurements and fit shows that the noise in our device is indeed composed of Hooge's low frequency and thermal contributions of the Wheatstone bridge. Above 5 V bridge bias, a similar detectivity is obtained whatever the bias in the *1/f* region, and in the white noise region the detectivity improves with the voltage bias as expected from Equation (10). Detectivity values close to the nT Hz$^{-1/2}$ range are obtained at 1 Hz with 5 V bridge bias at 310 K operating temperature, proving that our sensor is a viable candidate for biomedical applications. Above 1 kHz values as low as 240 pT Hz$^{-1/2}$ are achieved for the highest voltage bias. In the case of a 1 V bridge bias, the low frequency noise is dominated by the low frequency noise of the amplifier. This dominating contribution of the amplifier can be observed from the fact that in the low frequency domain the measured noise is the same at 0 V and 1V bridge bias.

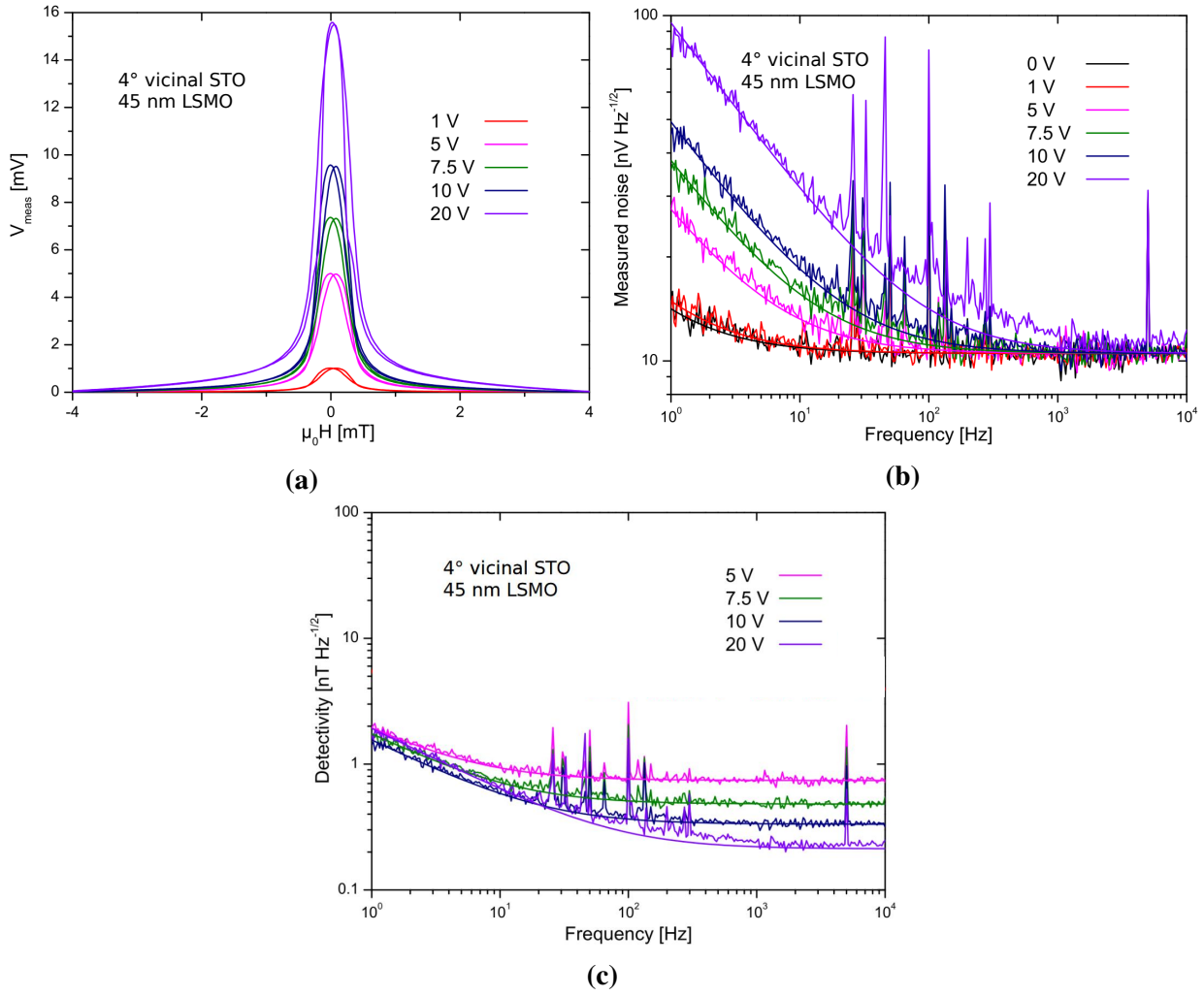

Figure 7. Characterization of optimized sample for different voltage bias at 310 K. a) $V_{meas}(H)$ curves show uniaxial behavior. b) Measured noise with fit using Equation (9) and taking into account the amplifier noise. c) Detectivity calculated from measured noise and obtained sensitivity.

3.3 Comparison with competing MR technologies

Apart from sensitivity and detectivity, other parameters have to be considered to describe any magnetic sensor and then evaluate its potential applications. We took into consideration the power consumption and the active area of the sensor. The value of all these parameters are listed in Table 2 for our LSMO sensor and for state of art GMR and TMR sensors. Concerning the low frequency noise, the relevant parameter is the $(S_v/V)^2$ parameter which can be expressed in a general expression $(S_v/V)^2 = K/f$. The expression for K varies from one sensor to the other and is either expressed as a function of the area of the sensing element for GMR and TMR sensor or

the volume for AMR sensor. For GMR and TMR sensors, data are available in literature for single elements or multiple elements connected in series or parallel. For a consistent comparison between sensors, the K values as well as the area, the power consumption and the detectivity of Wheatstone bridges structures made of single TMR and GMR sensing units, are provided in Table 2. These values are either directly available or can be calculated from reference [13,40] as well as the sensitivity and the detectivity for 1 V bias.

Clearly, the AMR sensor based on LSMO thin films provides an intrinsic low frequency noise lower by a few orders of magnitude. Although the sensitivity of our LSMO based AMR sensor is significantly less than the the one of GMR and TMR sensors, it has better performance at 1 Hz. At 1 kHz, the low 1/f noise is still dominating for GMR and TMR sensor while for LSMO AMR sensor the noise is limited by the thermal noise of the resistance value of the sensor. As a result, at 1 kHz its detectivity is slightly higher (worse) than the best GMR but a bit smaller (better) than the TMR sensors. As to the size and namely the occupied area of each sensor, the Wheatstone bridge AMR sensor presented in this paper is among the largest. Nevertheless, reducing the sensing area of the device can be done with an impact on the detectivity in the low frequency domain only. Any downscaling keeping the design unchanged would indeed keep the resistance unchanged and would thus keep the white noise and the detectivity unchanged in the white noise domain. As to the low frequency domain, limiting the downscaling by a factor to a few units would limit the reduction of the volume of the device and thus limit the degradation of the detectivity, which scales up as the inverse of the volume in the 1/f noise region, to the same factor. The power consumption of each sensor is related to the resistance value of each sensing element. It turns out from this comparison that the AMR sensor presented here have competitive characteristics compared to state of art TMR and GMR sensors which have been studied and developed for many years now. The facts that the $La_{2/3}Sr_{1/3}MnO_3$ AMR sensor has a simpler fabrication process, that it returns from saturation without any degradation of performance and that there is no need to worry about a possible loss of magnetization in a pinned layer also have to be pointed out.

Table 2. Characteristics of Wheatstone bridge structures made of single unit magnetoresistive sensors for 1 V bias. Note : the K value is extracted from the expression $(S_v/V)^2 = K/f$

Sensor Type	TMR[40]	GMR[13]	$La_{2/3}Sr_{1/3}MnO_3$ AMR
K	2.2×10^{-11} - 5.7×10^{-10}	3.4×10^{-14} - 3.4×10^{-12}	4.0×10^{-17}
S [% mT^{-1}]	1 - 2	1.3 - 3.0	0.1 - 0.3
D [nT $Hz^{-1/2}$] at 1 Hz	2400 - 240	12 - 610	5.0
D [nT $Hz^{-1/2}$] at 1 kHz	75 - 7.2	0.7 - 12	4.0
Area [μm^2]	60 - 5600	2.5×10^3 - 2.2×10^6	2.5×10^5
Power consumption [mW]	0.5 - 13.0	1.3	0.2

4 Conclusion

A single element magnetoresistive sensor based on a single epitaxial LSMO layer deposited over a vicinal substrate and etched in a Wheatstone bridge geometry was investigated. Our single layer device presents an intrinsic noise solely due to this single layer. The required uniaxial magnetic anisotropy in the LSMO single layer is obtained by the use of vicinal substrates, with a magnetization easy axis induced along the substrate step edges. MOKE imaging measurements show a reversible and coherent magnetization rotation when a magnetic field is applied perpendicular to the easy axis, and a Stoner-Wohlfarth magnetic energy model explains the experimental MR curves. For a given MR ratio, the sensitivity of our sensor is inversely proportional to the anisotropy field H_a of the film and its detectivity is proportional to H_a. We showed that it is possible to reduce H_a and thus improve sensor performance by tweaking three fabrication parameters: the vicinal angle of the substrate, the substrate temperature during PLD deposition and the LSMO film thickness. With a set of optimized fabrication parameters (45 nm thick film, 4° vicinal substrate, 730 °C deposition temperature), detectivity values as low as 1.43 nT $Hz^{-1/2}$ at 1 Hz and 240 pT $Hz^{-1/2}$ at 1 kHz were obtained for a single layer AMR sensor operating at body temperature. These are the lowest values reported for an AMR sensors based on manganite oxide. The performance above 1 kHz is comparable to multilayer devices that use metallic ferromagnetic materials such as GMR and TMR. Our sensor is quite simple to fabricate, easily scalable and avoids complex stacking of multiple layers. With the addition of flux concentrators in our sensor, a gain of one order of magnitude may be obtained,[41] and sub-nT detectivity even at 1 Hz can be expected. The novelty of using

vicinal substrates to induce in a controlled way an uniaxial magnetic anisotropy in oxide thin films can be applied to other low noise oxide with improved MR and conductance value. This could lead to MR magnetic sensors with further improved detectivity obtained with a simple fabrication process that avoids the precise control of multilayer deposition.

Acknowledgement

This project has received funding from the European Union Horizon 2020 research and innovation program under grant agreement No 737116. The work in Spain was supported by the Regional Government of Madrid and by the AEI through Projects P2018/NMT-4321 (NANOMAGCOST-CM), and PID2021-122980OB-C52 (ECLIPSE-ECoSOx), respectively. IMDEA Nanoscience Institute is supported by the "Severo Ochoa" Programme for Centres of Excellence in R&D, (MINECO grant SEV-2016-0686).

References

(1) Zheng, C. et al. Magnetoresistive Sensor Development Roadmap (Non-Recording Applications). *IEEE Transactions on Magnetics* **2019**, *55*, 1–30.

(2) Caruso, L.; Wunderle, T.; Lewis, C. M.; Valadeiro, J.; Trauchessec, V.; Trejo Rosillo, J.; Amaral, J. P.; Ni, J.; Jendritza, P.; Fermon, C.; Cardoso, S.; Freitas, P. P.; Fries, P.; Pannetier-Lecoeur, M. In Vivo Magnetic Recording of Neuronal Activity. *Neuron* **2017**, *95*, 1283–1291.

(3) Adachi, Y.; Oyama, D.; Kawai, J.; Kawabata, S.; Uehara, G. Spinal cord evoked magnetic field measurement using a magnetospinography system equipped with a cryocooler. *Conf Proc IEEE Eng Med Biol Soc* **2013**, 4426–4429.

(4) Jensen, K.; Skarsfeldt, M. A.; Stærkind, H.; Arnbak, J.; Balabas, M. V.; Olesen, S.-P.; Bentzen, B. H.; Polzik, E. S. Magnetocardiography on an isolated animal heart with a room-temperature optically pumped magnetometer. *Sci. Rep.* **2018**, *8*, 16218.

(5) Öisjöen, F. *High-Tc SQUIDs for Biomedical Applications: Immunoassays, Magnetoencephalography, and Ultra-Low Field Magnetic Resonance Imaging*; Springer, 2013.

(6) Körber, R. et al. SQUIDs in biomagnetism: a roadmap towards improved healthcare. *Supercond Sci Technol* **2016**, *29*, 113001.

(7) Broser, P. J.; Middelmann, T.; Sometti, D.; Braun, C. Optically pumped magnetometers disclose magnetic field components of the muscular action potential. *J Electromyogr Kinesiol* **2021**, *56*, 102490.

(8) Baibich, M. N.; Broto, J. M.; Fert, A.; Van Dau, F. N.; Petroff, F.; Etienne, P.; Creuzet, G.; Friederich, A.; Chazelas, J. Giant Magnetoresistance of (001)Fe/(001)Cr Magnetic Superlattices. *Phys. Rev. Lett.* **1988**, *61*, 2472–2475.

(9) Binasch, G.; Grünberg, P.; Saurenbach, F.; Zinn, W. Enhanced magnetoresistance in layered magnetic structures with antiferromagnetic interlayer exchange. *Phys. Rev. B* **1989**, *39*, 4828–4830.

(10) Julliere, M. Tunneling between ferromagnetic films. *Phys. Lett. A* **1975**, *54*, 225 – 226.

(11) Miyazaki, T.; Tezuka, N. Giant magnetic tunneling effect in Fe/Al_2O_3/Fe junction. *J. Magn. Magn. Mater.* **1995**, *139*, 231–234.

(12) Lei, Z. Q.; Li, G. J.; Egelhoff, W. F.; Lai, P. T.; Pong, P. W. T. Review of Noise Sources in Magnetic Tunnel Junction Sensors. *IEEE Trans. Magn.* **2011**, *47*, 602–612.

(13) Torrejon, J.; Solignac, A.; Chopin, C.; Doll, A.; Paul, E.; Fermon, C.; Pannetier-Lecoeur, M. Multiple Giant-Magnetoresistance Sensors Controlled by Additive Dipolar Coupling. *Phys. Rev. Appl.* **2020**, *13*, 034031.

(14) Silva, M.; Franco, F.; Leitao, D. C.; Cardoso, S.; Freitas, P. P. Two-dimensional arrays of vertically packed spin-valves with picoTesla sensitivity at room temperature. *Sci. Rep.* **2021**, *11*, 215.

(15) Guerrero, R.; Pannetier-Lecoeur, M.; Fermon, C.; Cardoso, S.; Ferreira, R.; Freitas, P. P. Low frequency noise in arrays of magnetic tunnel junctions connected in series and parallel. *J. Appl. Phys.* **2009**, *105*, 113922.

(16) Stutzke, N. A.; Russek, S. E.; Pappas, D. P.; Tondra, M. Low-frequency noise measurements on commercial magnetoresistive magnetic field sensors. *J. Appl. Phys.* **2005**, *97*, 10Q107.

(17) Henriksen, A. D.; Dalslet, B. T.; Skieller, D. H.; Lee, K. H.; Okkels, F.; Hansen, M. F. Planar Hall effect bridge magnetic field sensors. *Appl. Phys. Lett.* **2010**, *97*, 013507.

(18) Perna, P.; Rodrigo, C.; Jiménez, E.; Mikuszeit, N.; Teran, F. J.; Méchin, L.; Camarero, J.; Miranda, R. Magnetization reversal in half metallic $La_{0.7}Sr_{0.3}MnO_3$ films grown onto vicinal surfaces. *J. Appl. Phys.* **2011**, *109*, 07B107.

(19) Perna, P.; Maccariello, D.; Ajejas, F.; Guerrero, R.; Méchin, L.; Flament, S.; Santamaria, J.; Miranda, R.; Camarero, J. Engineering Large Anisotropic Magnetoresistance in $La_{0.7}Sr_{0.3}MnO_3$ Films at Room Temperature. *Adv. Funct. Mater.* **2017**, *27*, 1700664.

(20) Hemberger, J.; Krimmel, A.; Kurz, T.; Krug von Nidda, H.-A.; Ivanov, V. Y.; Mukhin, A. A.; Balbashov, A. M.; Loidl, A. Structural, magnetic, and electrical properties of single-crystalline $La_{1-x}Sr_xMnO_3$ $(0.4 < x < 0.85)$. *Phys. Rev. B* **2002**, *66*, 094410.

(21) Chuang, D. S.; Ballentine, C. A.; O'Handley, R. C. Surface and step magnetic anisotropy. *Phys. Rev. B* **1994**, *49*, 15084–15095.

(22) Lacour, D.; Jaffrès, H.; Nguyen Van Dau, F.; Petroff, F.; Vaurès, A.; Humbert, J. Field sensing using the magnetoresistance of IrMn exchange-biased tunnel junctions. *J. Appl. Phys.* **2002**, *91*, 4655–4658.

(23) Zhao, D.; Liu, F.; Huber, D. L.; G., L. M. Step-induced magnetic-hysteresis anisotropy in ferromagnetic thin films. *J. Appl. Phys.* **2002**, *91*, 3150.

(24) Goldberg, C.; Davis, R. E. New Galvanomagnetic Effect. *Phys. Rev.* **1954**, *94*, 1121–1125.

(25) West, F. G. Rotating-Field Technique for Galvanomagnetic Measurements. *J. Appl. Phys.* **1963**, *34*, 1171–1173.

(26) Haji-Sheikh, M. J.; Yoo, Y. An accurate model of highly ordered 81/19 Permalloy AMR Wheatstone bridge sensor against a 48 pole pair ring-magnet. *Int. J. Intell. Syst. Technol. Appl.* **2007**, *3*, 95–105.

(27) Tannous, C.; Gieraltowski, J. The Stoner-Wohlfarth model of ferromagnetism. *Eur. J. Phys.* **2008**, *29*, 475–487.

(28) Barone, C.; Pagano, S.; Méchin, L.; Routoure, J.-M.; Orgiani, P.; Maritato, L. Apparent volume dependence of 1/f noise in thin film structures: Role of contacts. *Rev. Sci. Instrum.* **2008**, *79*, 053908.

(29) Méchin, L.; Wu, S.; Guillet, B.; Perna, P.; Fur, C.; Lebargy, S.; Adamo, C.; Schlom, D. G.; Routoure, J. M. Experimental evidence of correlation between 1/f noise level and metal-to-insulator transition temperature in epitaxial $La_{0.7}Sr_{0.3}MnO_3$ thin films. *J. Phys. D* **2013**, *46*, 202001.

(30) Méchin, L.; Routoure, J.-M.; Mercone, S.; Yang, F.; Flament, S.; Chakalov, R. A. 1/f noise in patterned $La_{2/3}Sr_{1/3}MnO_3$ thin films in the 300–400K range. *J. Appl. Phys.* **2008**, *103*, 083709.

(31) Johnson, J. B. Thermal Agitation of Electricity in Conductors. *Phys. Rev.* **1928**, *32*, 97–109.

(32) Nyquist, H. Thermal Agitation of Electric Charge in Conductors. *Phys. Rev.* **1928**, *32*, 110–113.

(33) Hooge, F. $1/f$ noise is no surface effect. *Phys. Lett. A* **1969**, *29*, 139 – 140.

(34) Persson, A.; Bejhed, R.; Nguyen, H.; Gunnarsson, K.; Dalslet, B.; Østerberg, F.; Hansen, M.; Svedlindh, P. Low-frequency noise in planar Hall effect bridge sensors. *Sens. Actuator A Phys.* **2011**, *171*, 212 – 218.

(35) Saib, M.; Belmeguenai, M.; Mechin, L.; Bloyet, D.; Flament, S. Magnetization reversal in patterned in $La_{0.67}Sr_{0.33}MnO_3$ thin films by magneto-optical imaging. *J. Appl. Phys.* **2008**, *103*, 113905.

(36) Enger, L.-G. et al. Sub-nT Resolution of Single Layer Sensor Based on the AMR Effect in $La_{2/3}Sr_{1/3}MnO_3$ Thin Films. *IEEE Trans. Mag.* **2022**, *58*, 1–4.

(37) Wang, J.; Duan, H.; Lin, X.; Aguilar, V.; Mosqueda, A.; Zhao, G.-m. Temperature dependence of magnetic anisotropy constant in iron chalcogenide Fe3Se4: Excellent agreement with theories. *J. Appl. Phys.* **2012**, *112*, 103905.

(38) Belmeguenai, M.; Mercone, S.; Adamo, C.; Mechin, L.; Fur, C.; Monod, P.; Moch, P.; Schlom, D. G. Temperature dependence of magnetic properties of $La_{2/3}Sr_{1/3}MnO_3$ thin films on silicon substrates. *Phys. Rev. B* **2010**, *81*, 054410.

(39) Chaluvadi, S. K.; Ajejas, F.; Orgiani, P.; Lebargy, S.; Minj, A.; Flament, S.; Camarero, J.; Perna, P.; Méchin, L. Epitaxial strain and thickness dependent structural, electrical and magnetic properties of $La_0.67Sr_0.33MnO_3$ films. *J. Phys. D* **2020**, *53*, 375005.

(40) Monteblanco, E.; Solignac, A.; Chopin, C.; Moulin, J.; Belliot, P.; Belin, N.; Campiglio, P.; Fermon, C.; Pannetier-Lecoeur, M. Normalization and Correction Factors for Magnetic Tunnel Junction Sensor Performances Comparison. *IEEE Sens. J.* **2021**, *21*, 15993–15998.

(41) Zhang, X.; Bi, Y.; Chen, G.; Liu, J.; Li, J.; Feng, K.; Lv, C.; Wang, W. Influence of size parameters and magnetic field intensity upon the amplification characteristics of magnetic flux concentrators. *AIP Adv.* **2018**, *8*, 125222.